Journal of Dynamic Behavior of Materials
https://doi.org/10.1007/s40870-024-00436-8

S.I. : THADHANI

Effect of Dislocation Density on the Dynamic Strength of Aluminium

J. C. Jonsson[1] · D. J. Chapman[1] · L. Farbaniec[1] · E. M. Escauriza[1] · L. C. Smith[1] · D. E. Eakins[1]

Received: 11 December 2023 / Accepted: 17 July 2024

Abstract
The effects of cold work on dynamic flow strength is studied through measurements of dislocation density and elastic precursor attenuation in shocked aluminium. High-purity aluminium and Al 6082 alloy samples are subjected to up to three passes of rotary swaging, a severe plastic deformation (SPD) technique, in order to produce large variations in starting material conditions. Detailed material characterisation is performed using electron backscatter diffraction (EBSD) and transmission electron microscopy (TEM) to determine the initial dislocation density, texture, grain boundary density and misorientation distribution. Variations in dynamic strength are studied through the evolution of the elastic precursor amplitude with propagation distance in specimens with thicknesses between 0.2 and 1 mm, shock loaded to impact stresses of about 4.6 GPa. It is shown that dynamic strength decreases with increasing initial dislocation density in both materials, demonstrating rare, quantified measurements of a reversal in the effect of dislocation density on yield strength at strain rates around 10^4 s^{-1} and above.

Keywords Aluminium · Shock loading · Dynamic strength · Precursor decay · Severe plastic deformation · Dislocation density

Introduction

The attenuation of the elastic precursor wave with propagation distance is often studied as a means of probing the time-dependence of yield during high strain rate loading. Its decay rate is primarily ascribed to transient effects caused by dislocation movement and generation. Measurements of the propagation of the elastic–plastic wave in the weak shock regime has therefore become a highly valuable validation and calibration tool for dislocation-based models describing the dynamical strength of materials.

Recent iterations of such models have advanced to directly considering the underlying material microstructure, including the role of dislocation density [1–8]. It is now in many cases theoretically possible to account for the effects of processing history and microstructure during deformation. In continuum analytical theories, dislocations are treated using Orowan-based approaches [2, 9, 10] to predict the attenuation of the precursor wave. Other numerical microstructure-focused models go further to directly simulating interface velocimetry results [4–8], while dynamic discrete dislocation plasticity models aim to explicitly simulate the movement of populations of individual dislocations and their strain fields [3, 11, 12]. Theoretical results show that reducing the mobility of dislocations leads to a decrease in the decay rate of the elastic precursor amplitude, whereas an increase in the initial mobile dislocation density is shown to increase the decay rate. Few experimental studies however include detailed characterisation of the starting material state, especially that of the initial dislocation density. Models are too often compelled to rely on calibrated or estimated values, limiting these studies to fitting experimental observations rather than quantitatively predicting them [4].

In the limited cases where variations in initial dislocation density have been studied experimentally, the results have led to apparently contradictory conclusions. Observations of a decrease in the HEL after cold work have been made in studies on Ta [13–15], Ti [16, 17], Mg [18], Al 2024 and Al 1421 [17, 19]. Conversely, increases in the dynamic strength after cold work have been found in Fe [17], Cu [17], and in a wide range of other aluminium alloys [17, 19–22]. A

✉ J. C. Jonsson
jcz.jonsson@gmail.com

D. E. Eakins
daniel.eakins@eng.ox.ac.uk

[1] Department of Engineering Science, University of Oxford, Oxford OX1 3PJ, UK

Published online: 06 August 2024

consistent explanation for these conflicting behaviours is a goal of the present study, as it requires initial microstructural states and dislocation densities to be known in detail.

In this investigation, the evolution of the elastic precursor is studied in aluminium with varying degrees of swaging in samples ranging in thickness from 0.2 to 1 mm. Both 5N-Al and Al 6082-T6 are examined in order to examine role of initial dislocation density in a high-purity environment versus interactions in a precipitate-rich initial state. Emphasis is therefore placed on quantitatively determining the initial dislocation density, texture, grain boundary density and misorientation distribution through use of EBSD and TEM. The plate impact results along with the measured dislocation parameters are used to explore the effects of initial microstructure and the relative contributions of initial dislocation density on dynamic strength.

Experimental

Material Processing

The material used in the present study was obtained from commercially-sourced rods of 5N-Al ("five-nines" i.e. 99.999% pure Al) in the as-drawn state, and Al 6082-T6 with chemical composition as shown in Table 1, in the extruded state.

The 5N-Al was annealed for 1 h at 673 K to establish a baseline material state and reduce any effects of its processing history [23–25]. This resulted in recrystallised grains with an average size around 300 µm. The Al 6082-T6 was not annealed given that the tempered states are common forms in which the alloy is used, while annealing the alloy would instead significantly alter its material properties including the precipitation state of secondary phase particles. Both material rods subsequently underwent up to three passes of rotary swaging along the extrusion direction at ambient temperature. Samples are hereafter denoted as S0, S1 and S3 after 0, 1 and 3 passes respectively. The true strains, listed in Table 2, are here defined as,

$$\epsilon = \ln \frac{A_0}{A}, \tag{1}$$

where A_0 and A are the cross-sectional areas before and after swaging respectively (note the Al 6082 was subjected to twice the strain per swaging pass than the 5N-Al, a consequence of the starting diameters and available swaging dimensions).

Samples for EBSD and TEM were prepared from longitudinal and transverse sections of the rod respectively using electrical discharge machining (EDM). EBSD samples were further mechanically ground in a sequence of 400, 800, 1600 and 4000 grade SiC paper, followed by polishing using 9, 3, 1 µm diamond suspensions. Final surface polish was achieved using colloidal silica and ion polishing. The TEM samples were punched to 3 mm discs, thinned by mechanical grinding, and then ion-milled until perforation.

EBSD Characterisation

EBSD characterisation was performed with a Zeiss Merlin SEM equipped with a Bruker Quantax EBSD system and eFlash camera, operating at 20 kV. The step size of the EBSD scan was varied from 100 nm to 5 µm depending on the grain size of the specimens. Figures 1 and 2 show results collected from representative regions of samples with 0, 1 and 3 passes of swaging. High angle grain boundaries

Table I Chemical composition of the Al 6082-T6 alloy (wt%)

Al	Si	Fe	Cu	Mn	Mg	Zn	Ti	Cr
Bal	1.01	0.22	0.02	0.54	0.60	0.02	0.01	0.01

Table II Material properties of the 5N-Al and Al 6082 used in this study

Material	Swaging passes	True areal strain	Dislocation density (10^{13} m^{-2})	HAGB density (µ m^{-1})	LAGB density (µ m^{-1})	Vickers hardness
5N-Al S0	0	0	0.4 ± 0.1	0.007	0.013	20
5N-Al S1	1	0.5	5.3 ± 1.6	0.012	0.058	21
5N-Al S3	3	1.4	11.2 ± 3.4	0.042	0.126	24
Al 6082 S0	0	0	12.9 ± 3.9	0.241	0.229	106
Al 6082 S1	1	1	38.7 ± 11.7	0.626	1.023	113
Al 6082 S3	3	2.8	29.2 ± 8.8	4.119	2.575	122

Sample types are designated as S0, S1, and S3 for 0, 1 and 3 swaging passes respectively. Dislocation densities are estimated from TEM measurements, and grain boundary densities are estimated from EBSD results

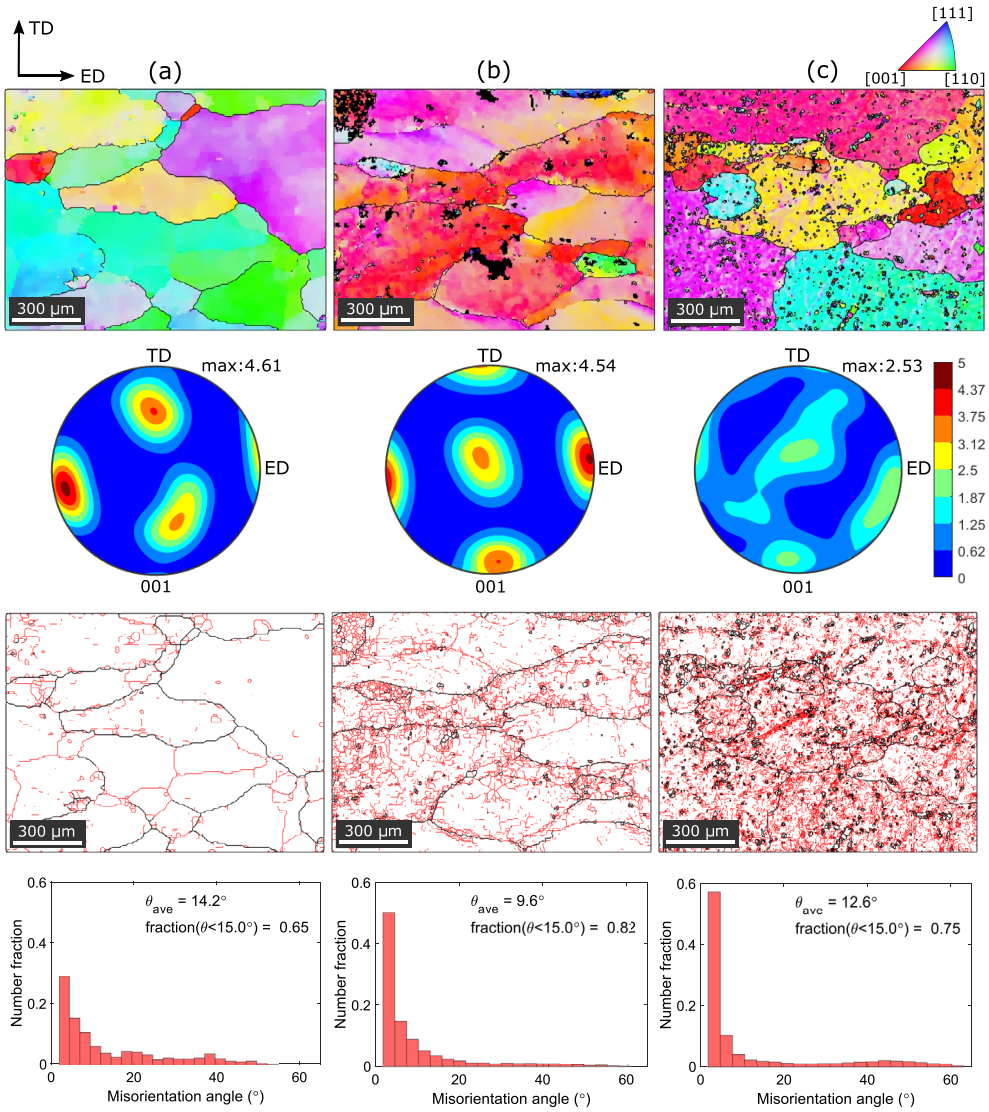

Fig. 1 EBSD IPF maps, pole figures, boundary maps and boundary misorientation distributions in 5N-Al of the **a** annealed, **b** 1 pass swaged, and **c** 3 pass swaged material. Swaging was applied along the extrusion direction

(HAGB) are defined by a misorientation of > 15°, and low angle grain boundaries (LAGB) by misorientations of 2–15°, shown as black and red lines respectively in the grain boundary plots.

The microstructural morphology is observed to consist primarily of coarse grains elongated along the extrusion direction, interspersed by finer equiaxed grains of sizes < 10 µm for the 5N-Al and <1 µm for the Al 6082. In the 5N-Al, the initial thickness of the elongated grains is approximately 300 µm. After 1 and 3 swaging passes, the size of the coarse grains remains similar, however the material becomes heavily populated with small equiaxed grains with an average size of 11 µm for S1 and 5 µm for S3. In the Al 6082 alloy, the starting material exhibits a very strong fibrous structure along the swaging direction. The initial thickness of the elongated grains is approximately 9 µm, which is reduced to 4 µm and 3 µm for S1 and S3 respectively. The S1 and S3 states also have significant populations of ultrafine grains (UFGs) with an average size of around 600 nm in both cases. The increasing fraction of unindexed (black) regions with number of swaging passes found between the boundaries of the coarse grains also suggests an increased accumulation of low angle grain boundaries and very high dislocation densities.

Listed in Table 2 are the resulting boundary densities, calculated as $\rho_{GB} = L/A$, where L is the total length of boundaries and A is the total area of the scan. The boundary density increases rapidly with increasing swaging, as is also evident from the boundary plots in Figs. 1 and 2. The corresponding misorientation distribution histograms show that the LAGB

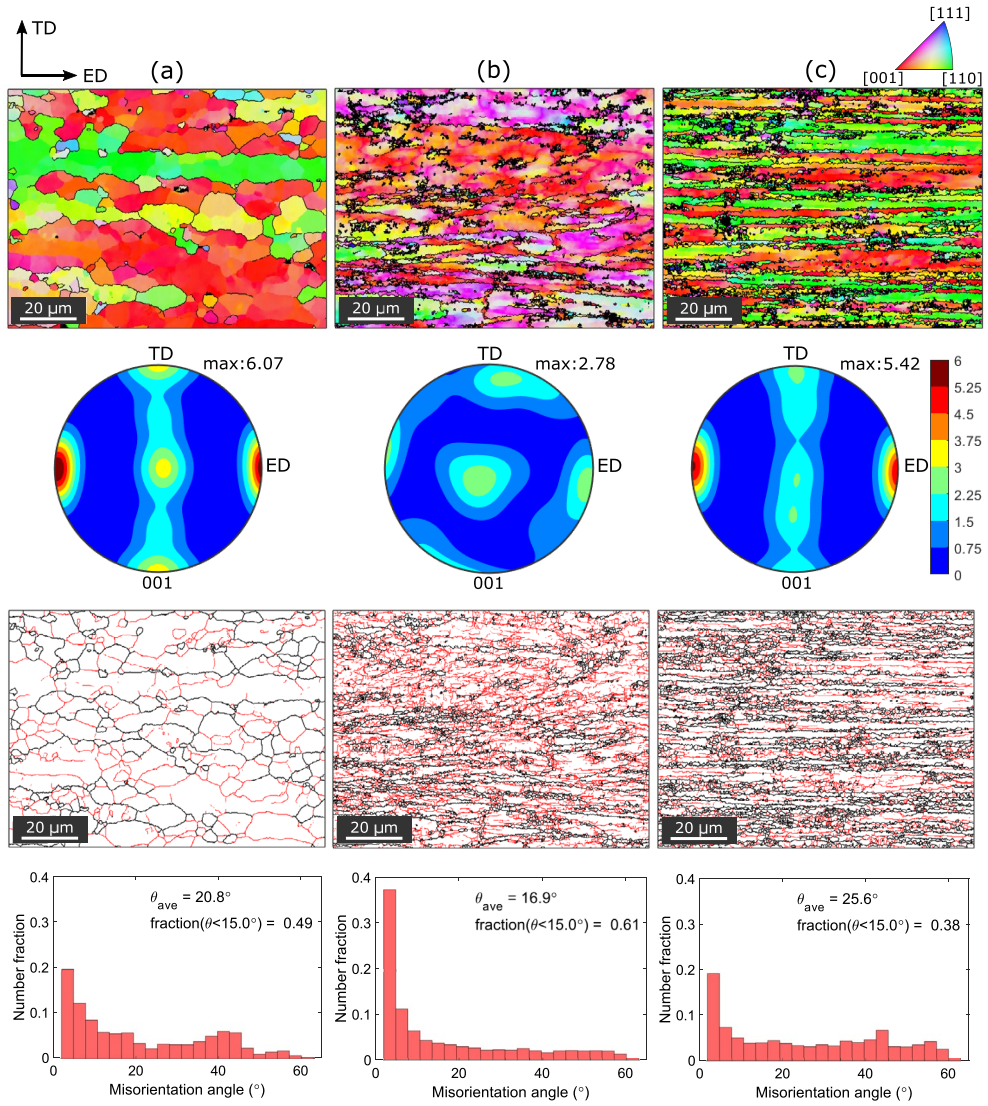

Fig. 2 EBSD IPF maps, pole figures, boundary maps and boundary misorientation distributions in Al 6082 of the **a** as-received, **b** 1 pass swaged, and **c** 3 pass swaged material. Swaging was applied along the extrusion direction

density reaches a peak at strains between 0.5 and 1.4 (samples 5N-Al S1, S3 and Al 6082 S1). The increased misorientation within the grains and the formation of subgrains is evidence of the large increase in dislocation density, as dislocation tangling promotes the formation of LAGBs [25]. However, at the highest studied strain of 2.8 in Al 6082 S3, it is observed that the fraction of LAGB is decreased to below that of the as-received material. It is likely that the dislocation density has started reaching a saturation level in which continued straining causes annihilation of dislocations at the LAGBs, which simultaneously causes an increase in the grain misorientation angles [25, 26].

The sequence of grain rotations is also evident from analysis of the pole figures. The ⟨001⟩ poles in the initial state are preferentially oriented along the extrusion direction. However, after swaging to strains of 1 and 1.4, significant grain rotation has occurred and the crystallographic orientations are more randomised. Finally, at a strain of 2.8 in the Al 6082 S3, the ⟨001⟩ axes have once again become preferentially oriented along the swaging direction, similar to the S0 state, showing evidence of LAGBs consolidating into HAGBs.

TEM Characterisation

TEM imaging was carried out with a JEOL JEM-2100 operating at 200 kV. Specimen thicknesses were measured to be 70–130 nm using EELS. Dislocation densities were estimated using the linear intercept method [27] and are listed in Table 2, where the error is dominated by the

uncertainty in the thickness computation of the foils. The dislocation densities presented here are in excellent agreement with pure Al and Al 6082 processed by other SPD methods [28–31].

Representative TEM bright-field images from the 5N-Al are shown in Fig. 3. The S0 sample displays a dislocation density on the order of 10^{12} m^{-2}, indicative of an annealed material with a prior history of extrusion which has partially recovered but not fully recrystallised [30, 32]. Very few grain boundaries are observed, reflecting the large grain size and low boundary density also found in the EBSD analysis. After the first swaging pass, the material displays a significant increase in dislocation density. A typical cellular substructure is observed including dislocation pile ups showing evidence of subgrain boundary formation, with low dislocation densities at the cell interiors [33]. Similar substructure in swaged Al 1070 has been found by Yang [34] and in pure Al by El-Madhoun [35]. After 3 passes, grain refinement has progressed substantially. Many of the dislocation sub-boundaries produced at lower strains have formed ultrafine grains with high angle boundaries. Dislocation densities have reached above 10^{14} m^{-2}, similar to pure Al processed through accumulative roll bonding (ARB) [30], with frequent dislocation tangles observed inside grain interiors.

In the Al 6082, shown in Fig. 4, the starting as-received material displays an already high dislocation density, as anticipated from an extruded precipitation-hardened alloy, as well as a substantial presence of second-phase Mg_2Si particles [36, 37]. As the effect of precipitates is to trap dislocations and prevent absorption at grain boundaries, the alloy exhibits a smaller relative proportion of mobile dislocations and a higher density between boundary walls than the pure Al. In the 1 pass Al 6082, individual dislocations are no longer easily distinguishable at the lower magnifications shown in the figure, with observation of heavy dislocation tangling similar to other SPD processed Al 6082 [38–40]. The highly tangled region shown in Fig. 4b is estimated to have a dislocation density of around 7×10^{14} m^{-2}.

Further grain refinement is evident after 3 passes, showing a high fraction of sub-micron sized and even nanostructured grains with very high densities of internal dislocations. However, the overall dislocation density has decreased compared to S1. This is likely a consequence of the material reaching a saturation stage where hardening is balanced by recovery mechanisms. It has indeed been reported that continued heavy plastic deformation leads to a saturation stage in grain refinement where further straining can instead cause grain coarsening and dislocation annihilation [41].

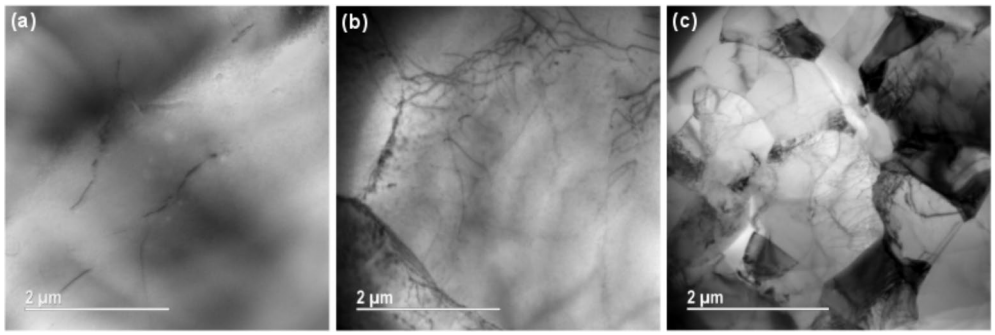

Fig. 3 TEM micrographs of the **a** as-received, **b** 1 pass swaged, and **c** 3 pass swaged 5N-Al

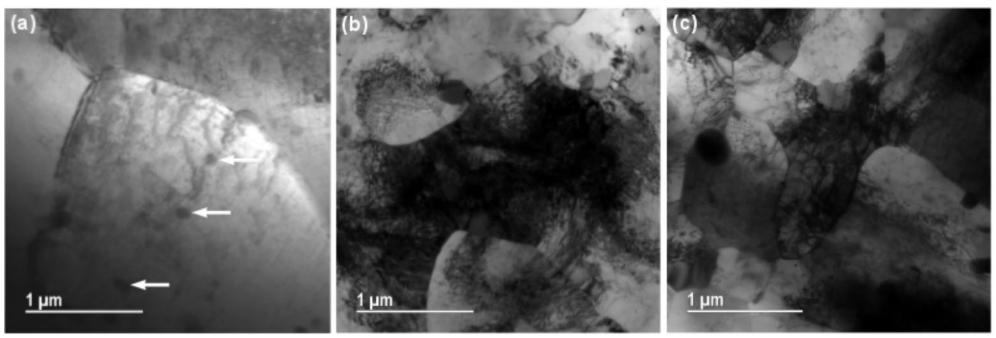

Fig. 4 TEM micrographs of the **a** as-received, **b** 1 pass swaged, and **c** 3 pass swaged Al 6082. Second-phase Mg_2Si particle shown with white arrows

The evolution of misorientation distributions and formation of ultrafine-grains observed in the EBSD measurements suggests a high degree of dislocation absorption into HAGBs. The low melting temperature and high stacking-fault energy of aluminium also makes dislocation annihilation through dynamic recovery likely [26, 30]. In this high strain regime, dislocation multiplication due to continued straining is therefore overshadowed by annihilation and grain boundary migration. Indeed, up to order-of-magnitude decreases in dislocation density after reaching the saturation stage have been observed in ARB processed aluminium [42] and in ECAP processed copper [43].

Experiment Assembly

Targets for plate impact experiments were sectioned transverse to the extrusion direction using EDM. High flatness and parallelism in the targets discs, necessary to avoid ramp-effects caused by impact tilt, was achieved by diamond turning both sides of the targets to the final thicknesses listed in Table 3. The resulting parallelism was < 0.1 mrad. C-cut sapphire, with a surface planarity of < 0.2 mrad, was used as both flyer and driver. The back free surface of the driver and the front surface of the flyer was flash coated with <100 nm of Al to allow optical measurement of shock arrival time and impact velocity, respectively. The Al targets were adhered to the sapphire drivers using a spin-coating method in which a glue layer, measured to < 1 µm thick, is first deposited on the driver, after which the target is bonded to the assembly. This ensured a thin and even glue layer, minimising the effects of tilt or glue layer ring-up. A 32 mm bore single stage gas gun was employed to dynamically load the final target assembly, shown in Fig. 5, at impact velocities of 400 m/s and vacuum levels below 50 mtorr. Photon Doppler Velocimetry (PDV) operating at a base frequency of 4 GHz [44] was used to measure the velocity histories of the target, driver and flyer.

Results

A series of 22 impact experiments, listed in Table 3, were conducted at target thicknesses from 0.2 mm to 1 mm for all three swaging levels of both the 5N-Al and Al 6082. The impact velocity of 400 m/s corresponded to a peak shock stress of about 4.6 GPa in the aluminium. PDV spectrograms were processed using STFT methods [45] with a window length of 64 points and 50% overlap, corresponding to 0.8 ns time-steps. Velocity histories were computed from Gaussian fits to the power spectrum for each time-step.

The combined wave profiles for the impact experiments are shown in Figs. 6 and 7, with thicknesses indicated in the figures. The breakout times of the shock waves have been shifted for clarity. The velocity profiles reveal clear

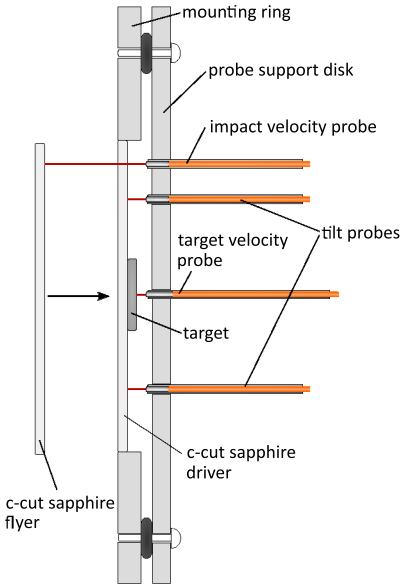

Fig. 5 Experimental configuration for the single stage gas gun shots. The velocity of the target free surface is measured using frequency-shifted PDV. The impact velocity of the projectile is measured through a window in the driver. The tilt and time of arrival of the shock at the target front surface is determined from PDV measurements at three equidistant points on the sapphire driver

precursor waves without peaks, followed by the principal plastic wave. Note that experiment 2 is not plotted as it was a repeat of experiment 1 and displayed a near identical velocity response. Significant decay of the elastic precursor with propagation distance is exhibited in the 5N-Al, whereas only very slight precursor attenuation is observed in the Al 6082. This is in agreement with the numerous previous studies on both pure Al and the very similar Al 6061 alloy. To make a direct comparison, the peak elastic stresses, σ_y, listed in Table 3 were calculated from the standard expression,

$$\sigma_y = \frac{1}{2}\,\rho_0\, c_l\, u_{fs}, \tag{2}$$

where ρ_0 is the unshocked mass density, c_l is the longitudinal sound speed, and u_{fs} is the free surface velocity at the precursor peak. Note that the yield point has been denoted as σ_y, rather than the commonly used σ_{HEL}, to distinguish these evolving peak elastic stress measurements from the "far-field" or equilibrium HEL stress of the precursor wave (after attenuation has taken place). Densities used were 2.70 ± 0.01 g/cm^3 for the 5N-Al and 2.71 ± 0.01 g/cm^3 for the Al 6082. The longitudinal sound speed was taken as 6.4 ± 0.1 mm/µs for both materials [46, 47].

In Fig. 8, the peak elastic stresses are plotted against propagation distance (or sample thickness, t) alongside literature data from a mixture of gas gun and laser shock experiments on both pure Al and Al 6061. The results

Table III Experimental parameters of the impact experiments on 5N-Al and Al 6082

Expt no	Material	Swaging passes	Sample thickness (μm)	Impact velocity (m/s)	Peak elastic stress (GPa)
1	5N-Al S0	0	200 ± 5	399 ± 1	0.435 ± 0.027
2	5N-Al S0	0	202 ± 1	400 ± 1	0.440 ± 0.027
3	5N-Al S0	0	403 ± 1	397 ± 1	0.237 ± 0.026
4	5N-Al S0	0	539 ± 1	399 ± 1	0.235 ± 0.026
5	5N-Al S0	0	609 ± 1	393 ± 1	0.180 ± 0.026
6	5N-Al S0	0	1031 ± 5	426 ± 1	0.164 ± 0.026
7	5N-Al S1	1	200 ± 5	400 ± 1	0.405 ± 0.027
8	5N-Al S1	1	405 ± 1	398 ± 1	0.241 ± 0.026
9	5N-Al S1	1	586 ± 1	396 ± 1	0.173 ± 0.026
10	5N-Al S1	1	1015 ± 1	396 ± 1	0.153 ± 0.026
11	5N-Al S3	3	200 ± 1	404 ± 1	0.383 ± 0.027
12	5N-Al S3	3	408 ± 1	393 ± 1	0.178 ± 0.026
13	5N-Al S3	3	1002 ± 1	406 ± 1	0.108 ± 0.026
14	Al 6082 S0	0	203 ± 5	414 ± 1	0.932 ± 0.030
15	Al 6082 S0	0	404 ± 5	402 ± 1	0.835 ± 0.029
16	Al 6082 S0	0	968 ± 5	409 ± 1	0.722 ± 0.029
17	Al 6082 S1	1	195 ± 5	398 ± 1	0.731 ± 0.029
18	Al 6082 S1	1	402 ± 5	405 ± 1	0.731 ± 0.029
19	Al 6082 S1	1	968 ± 5	407 ± 1	0.568 ± 0.028
20	Al 6082 S3	3	183 ± 5	402 ± 1	0.829 ± 0.029
21	Al 6082 S3	3	401 ± 5	403 ± 1	0.857 ± 0.029
22	Al 6082 S3	3	888 ± 5	396 ± 1	0.720 ± 0.029

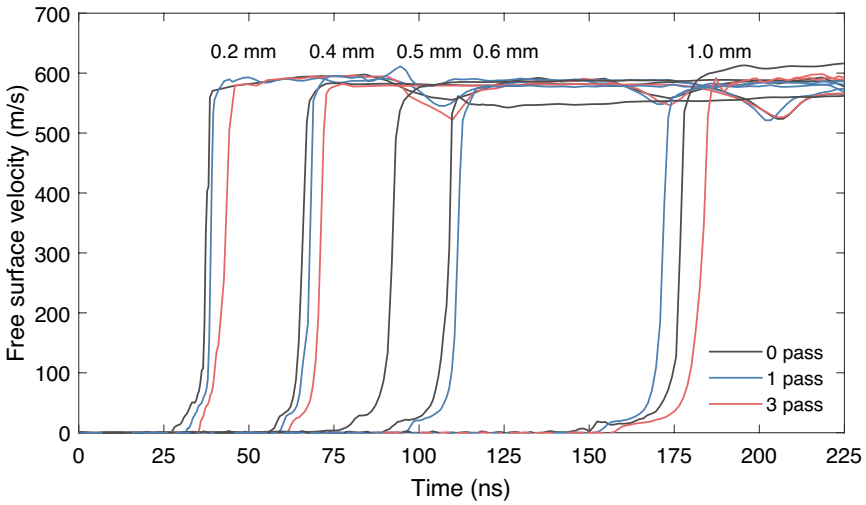

Fig. 6 Pure Al velocity profiles

along with the previous data have been fitted to power laws of the form $\sigma_y = \sigma_0 t^n$, where σ_0 and n are the fitting parameters. Good agreement is found between the yield points of the annealed 5N-Al and the pure aluminium from previous studies, whereas the as-received Al 6082 has slightly higher yield points than the Al 6061 in the studied thickness range. More notable are the significant differences in the yield points of the S0, S1 and S3 samples at constant thickness in both of the present materials. A monotonic decrease in peak stress with increasing swaging passes (up to a true strain of 1.4) is observed in the 5N-Al at all thicknesses. Tied with the measured increase in dislocation density, this is indicative of the dominant role played by mobile dislocations at high strain-rates in determining the rate of stress relaxation at the onset of plastic flow. Interestingly, in the case of the Al 6082, the first swaging pass is associated with a decrease in the strength, whereas after the third swaging pass there is a reversal in which

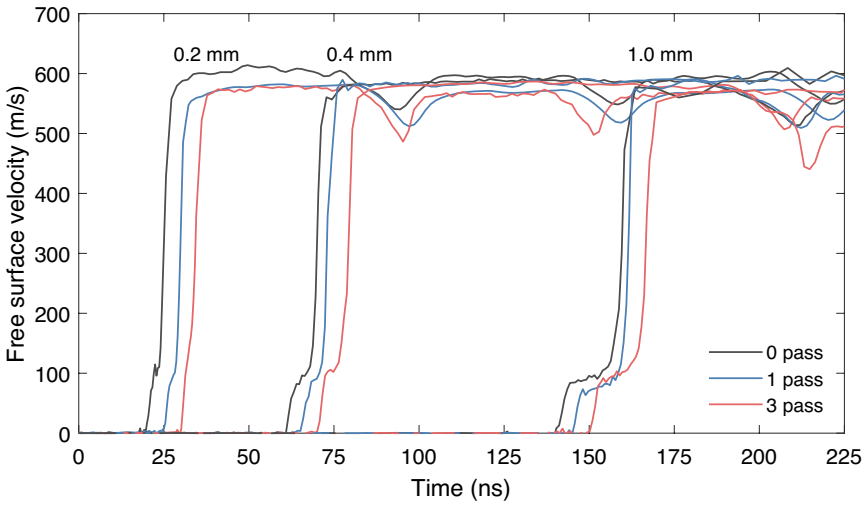

Fig. 7 Al 6082 velocity profiles

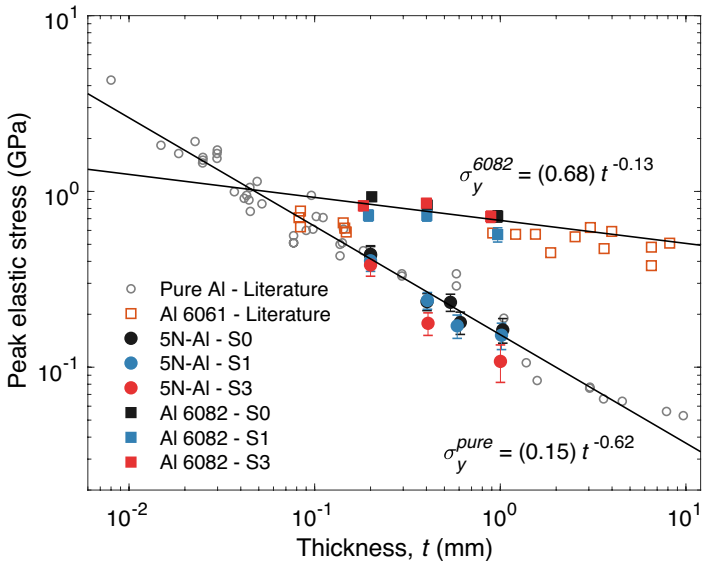

Fig. 8 Peak elastic stress in 5N-Al and Al 6082 plotted against propagation distance comparing present results to literature data [48–55]

the dynamic strength reverts back towards that of the unswaged material. It should be noted that the Al 6082 was taken to a higher strain than the pure Al.

The initial longitudinal plastic strain rate is calculated using [52],

$$\dot{\epsilon}_p = \frac{du_p/dt}{c_l} \equiv \dot{\epsilon}_p|_{u_{E,Min}}^{2u_{E,Min}}, \tag{3}$$

where u_p is the particle velocity and $u_{E,Min}$ is the particle velocity at the peak of the elastic wave. The strain rate is calculated from the onset of plasticity at $u_{E,Min}$, up to $2 \times u_{E,Min}$, which is taken as indicative of the plastic strain rate experienced at the elastic limit. A strong correlation is found between the strain rate and the dynamic yield stress, shown in Fig. 9, in which the results have again been fitted to power laws as shown in the figure. The fit for the 5N-Al compares favourably to the equivalent fit of $(0.001)\dot{\epsilon}_p^{0.43}$ found by Smith et al. [52]. Sharp up-turns in the flow stress have been found above $10^3 s^{-1}$ for pure Al [56], associated with a transition into the currently shown region of strong strain rate dependency. This represents the regime in which phonon drag effects are dominant over thermal activation, meaning mobility is limited by the drag force caused by resistance of the lattice to motion [33]. Dislocation drag is a manifestation primarily of phonon scattering and radiation by dislocations, which are effects known to be proportional to temperature. Indeed, experiments by Zaretsky and Kanel on pure Al at 900K showed an increase of the HEL by 4–5 times compared to room temperature, at thickness ranges of 0.1–2 mm [47].

The Al 6082 displays a much lower strain rate sensitivity compared to the pure Al. In these cases, materials

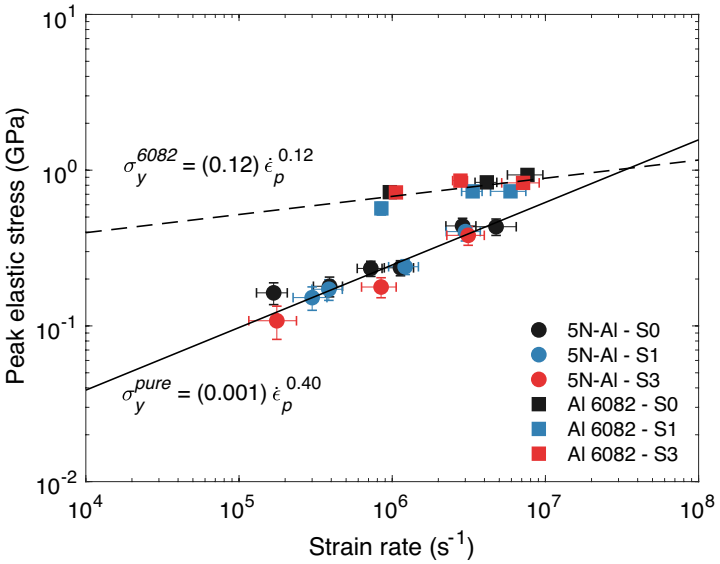

Fig. 9 Peak elastic stress in 5N-Al and Al 6082 plotted against strain rate. The data points are fitted to power laws as displayed in the figure. It is found that the pure aluminium displays a significantly higher strain rate sensitivity than the alloy. The addition of secondary phase particles shifts the aluminium from the phonon drag to the thermal activation regime at these strain rates

with secondary phase particles and/or higher Peierls barriers (such as the present alloy or BCC metals) will present greater obstacles to dislocation movement, which increases the shear stress needed to induce plastic flow and therefore the magnitude of the peak elastic stress. This decreases the strain rate dependence by shifting the material into the thermal activation regime. It is believed that if the strain rate was increased above $10^7 s^{-1}$, or equivalently the thickness decreased below 200 µm, only then would phonon drag effects drive significant increases to the peak elastic stress. Zaretsky et al. investigated this threshold more closely in a series of impact experiments on Al 6061, in which it was found that the strain rate needed to reach the transition to the phonon drag regime increases dramatically with higher aging time (precipitation hardening) [57].

Discussion

The relationship between peak elastic stress and dislocation density is demonstrated more clearly in Fig. 10. In the 5N-Al, a decrease is observed in the elastic peak with increasing dislocation density and swaging passes at all thicknesses. In the Al 6082, since the dislocation density of the S3 sample is lower than S1, again the result is a trend of decreasing elastic stress with increasing dislocation density for all thicknesses. This proves a counter-intuitive inverse relationship between strength and dislocation density at high strain rates. In the annealed material, the high precursor states in the attenuation region are a result of the failure of dislocation mobility alone to relax the imposed deviatoric stresses, causing a high dependence on dislocation generation. In the cold worked material however, the experimental results suggest that the higher availability of initial mobile dislocations is responsible for increased stress relaxation in the swaged samples and a lessened reliance on generation mechanisms.

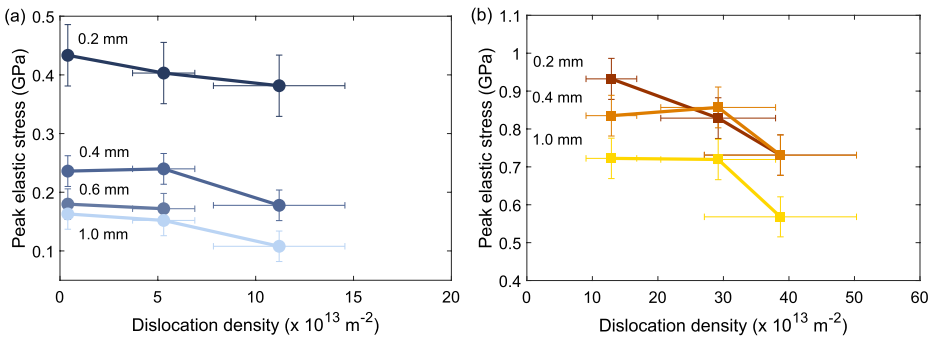

Fig. 10 Peak elastic stresses from the **a** 5N-Al and **b** Al 6082 plate impact experiments, plotted against dislocation density. Thicknesses are shown in the figure, with experiments at the same thickness connected by lines. A decrease in the yield point is observed with increasing dislocation density in both materials

Similar observations of a decrease in yield point after cold working have been made in studies on tantalum [13–15]. Razorenov et al. compared the dynamic strength of UFG tantalum and coarse grained tantalum, finding it to be lower in the UFG Ta [14]. They theorised that the increase in grain boundary density in the UFG material led to a higher rate of stress-relaxation caused by increased dislocation nucleation at the grain boundaries. In the study by Millett, the difference was quite pronounced as the material displayed a peak-and-valley profile in the as-received state, which turned into the more diffuse shoulder-type yield point after cold working [13]. The material was only cold rolled up to a strain of 0.5 and can therefore not be considered SPD processed. Although dislocation densities were not measured directly, TEM data indicated that differences in total dislocation density was likely not as large as the present study. Despite this, the cold rolled samples had lower yield points than the as-received material even up to the very high propagation distance of 9 mm. It was theorised that the cold-rolling process resulted in a displacement of dislocations away from surrounding interstitial solute atoms which ordinarily would have acted as pinning points. Consequently, even if the total dislocation density change was comparatively small, there was a significant increase in the ratio of mobile versus immobile dislocation densities, thus causing a faster decay rate. Decreases in yield strength in cold worked tantalum was also found in work by Asay et al. [15], who drew similar conclusions. Zaretsky and Kanel found that annealed Ta had a higher yield point than the as-rolled material [58], prompting them to suggest that defects which ordinarily strengthen the material instead act as sources of mobile dislocations at high strain rates.

Decreases in the yield point after cold work has also been observed in Al 2024 and Al 1421 [17, 19], however conflicting results have been found in other aluminium alloys. In a study on Al 5083, high pressure torsion (HPT) was applied to produce a UFG structure with accumulated strains up to 9.3 [19]. Shock wave experiments performed on coarse grained (CG) samples in the initial annealed state resulted in a yield point of 0.4 GPa, whereas the UFG state had much higher yield around 0.8 GPa, both at 1 mm thickness (i.e. opposite trend to the current 1 mm data). Note that the yield point of the initial material was quite low compared to present results.

Similarly, a study comparing CG to ECAP processed Al 6063 led to peak elastic stresses of 0.2 and 0.4 GPa for the CG and UFG materials, respectively, at 2 mm propagation distance [17]. Again however the reported yield point of only 0.2 GPa for the CG material is very low for an aluminium 6000-series alloy (expected to be around 0.6 GPa as shown in Fig. 8). Supplementary data from the ECAP processed Al 6063 study, discussed by Razorenov [19], displayed very significant attenuation of the precursor stress at thicknesses all the way up to 8 mm. This is again inconsistent with data from similar alloys in which the precursor amplitude is almost fully decayed by 0.2 mm. This is likely related to the processing history, which was reported as an annealing step followed by aging [59]. Similar results showing cold work strengthening at high strain rates were found in dynamic channel angular pressing (DCAP) processed aluminium alloys A7, 7075, 3003, 5083 [20, 60], ARB processed Al 1070 [21], and ECAE then cold rolled Al 5083 [22, 61]. In the ARB study, the initial cycles caused an increase in the yield point, which then peaked and eventually decreased. In the ECAE study, no large difference was observed after the initial pass, and only after subsequent cold rolling did the yield point start to increase. In all of the above mentioned studies, the initial reference alloy was annealed to varying degrees prior to applying the cold working method.

A likely explanation of the apparent inconsistency between these studies and the current data lies within the material processing histories. Studies by Zaretsky et al. showed that annealing Al 6061-T6 produces an up to three-fold reduction in the peak elastic stress [47, 57]. Each subsequent stage of the precipitation sequence is then accompanied by an increase in the shear stress required for dislocation unpinning. As expected however, Zaretsky and Kanel found that the annealed then paritally aged alloy samples would still display significantly reduced strength compared to original conditions. At 1 mm thickness, the partially aged 6061 exhibited peak elastic stresses of only 0.3 GPa, compared to 0.6 GPa of fully age-hardened 6061 in the T6 state. At higher propagation distances, the yield points of the annealed samples continue to attenuate down to 0.15 GPa at 6 mm thickness (compared to 0.5 GPa for 6061-T6).

It is therefore clear that the strengthening effects of alloying elements and their exact precipitation state in the material has immense repercussions on the yield point, as is also emphasised by the large differences in dynamic strength between pure aluminium and its alloys. It is likely that this pattern of strengthening was at play in the previous studies on cold worked aluminium alloys discussed above, where annealing was followed by a combination of cold working and aging (of which the latter occurs even at room temperature in both e.g. the 2000 and 7000 series alloys [62]). First, by annealing to the solid solution state, the dynamic yield point is reduced by a factor of 2 to 3 compared to the same material in the fully precipitation hardened state. Next, while subsequent cold work causes an increase in the dislocation density, the character of these new dislocations is likely heavily weighted towards immobile rather than mobile dislocations (in particular when compared to cold working a pure material). This, combined with a potential increase in the unpinning stress caused by aging, overshadowed any softening effect caused by increases in mobile dislocations.

The present TEM data in Figs. 3 and 4 points towards this distinction in the type of dislocations created through cold working pure versus alloyed material. After swaging to the S1 state, the pure aluminium has developed a cellular substructure with low dislocation densities at the cell interiors. Such microstructure is indicative of highly mobile dislocations and a high SFE [63, 64]. In the Al 6082 on the other hand the grain interiors are densely populated with randomly spread immobile dislocations, likely due to the substantial presence of second-phase Mg_2Si particles preventing dislocation movement and absorption at grain boundaries during deformation. This is supported by the study on Al 2024 [17], in which the initial fully age hardened material was compared to the annealed and the UFG states, with resulting peak elastic states of 0.73, 0.19 and 0.32 GPa, respectively. Again it was shown that annealing results in a large decrease in strength, and while the UFG state did exhibit a higher yield point than the annealed sample, it was low when compared to the fully age hardened material. This general trend seems to be consistent with the above findings, however exact quantification of microstructures is needed.

It is noted that the EBSD results in Figs. 1 and 2 display significant changes in texture which may have influenced yield points, particularly for the Al 6082 measurements. Previous studies by Owen [65] and Huang [66] have shown small variations in the dynamic strength of single crystal aluminium depending on loading direction. The relative strengths of these loading angles can be explained by an orientation-based calculation of the ratio between the maximum resolved shear stress in the $\{111\}\langle 1\bar{1}0\rangle$ slip planes and the applied longitudinal stress. Such calculations have been used before to calculate the resolved shear stress in the elastic wave under uniaxial strain conditions at arbitrary loading angles [9, 67], and was recently used by the present authors to analyse the effect of orientation distribution on the predicted strength of textured Mg AZ31 [68]. A similar analysis was also employed here, in which the area-weighted average Schmid factors (m) were calculated for all samples from the EBSD results [69]. For 5N-Al S0, S1 and S3 this led to $m =$ 0.48, 0.47, and 0.45 respectively, while for Al 6082 S0, S1, and S3 the results were m = 0.44, 0.44, 0.43 respectively. In the S0 material states, the spread of loading angles is close to the [100] axis which is highly favourable for maximising the resolved shear stress in the $\{111\}\langle 1\bar{1}0\rangle$ slip planes, resulting in high average Schmid factors. In contrast, while the 5N-Al S3 and Al 6082 S1 also display grains in similarly favourable orientations, a very significant population of grains have been reoriented with the [111] axis towards the impact direction. As this is the highest strength orientation, the expected effect is to balance or potentially even increase the yield point of these samples when compared to S0 (given the overall decrease in Schmid factors). The indication from these results therefore is that it is unlikely that the observation of a lower yield point is driven by the change in orientation distribution.

Similarly, it is possible that changes in grain boundary density may have either contributed to the reduction in peak elastic stress, by serving as points of facilitated dislocation nucleation, or counteracted it through grain boundary strengthening. However, previous studies on aluminium have found that even order of magnitude differences in grain size has led to no significant impact on dynamic strength [52, 70–72]. In recent experiments by Asay et al., pure aluminium was cold rolled and then annealed at varying temperatures in order to produce a range of grain sizes from 49 to 453 µm, finding that the dynamic strength was insensitive to the initial conditions. A similar study by Huang et al. on a variety of initial grain sizes in pure Al (180–300 µm) and Al 6061 (5–50 µm) also showed no clear indication of a grain size dependent response. While grain boundary effects should not be ruled out, they are likely secondary to the effects of initial dislocation density under the present conditions.

The above observations are summarised in Fig. 11, showing the effects of pre-straining a material through cold work prior to high and low strain rate loading. At low to intermediate strain rates of up to around 10^3 s^{-1} [73], cold work is well-known to result in improved strength due to higher dislocation densities causing increased resistance to dislocation glide. In the high strain rate regime (above around 10^5 s^{-1}), the opposite behaviour has been exhibited. At these strain rates, the availability of mobile dislocations is highly dominant in determining the rate of stress relaxation. Increasing the initial dislocation density addresses the lack of mobile dislocations in the attenuation stage immediately following impact, resulting in lower yield points. The experimental evidence suggests this is the case both for pure materials and age hardened alloys. Finally, in the special case when an aluminium alloy is annealed, the behaviour is altered in the high strain rate regime because of the exceedingly dominant role played by the alloying elements. Having initially been annealed, the dynamic strength in the "reference" state of these alloys is at its low point. Subsequent cold work likely leads to several order of magnitude increases in pinned and immobile dislocations, as well as increases in the unpinning stress caused by aging. Consequently, the overall yield stress increases despite any additions in mobile dislocation density.

While dynamic yield is a complex interplay between the state of alloying elements, initial mobile and immobile dislocations, nucleation at grain boundaries and more, the degree to which these factors can be measured and compared during shock loading through experimental techniques has its limitations. Future confirmation of the above hypotheses will require the use of models in which each of these components can be parameterised, allowing the relative influence of these factors to be simulated. Models in which initial dislocation

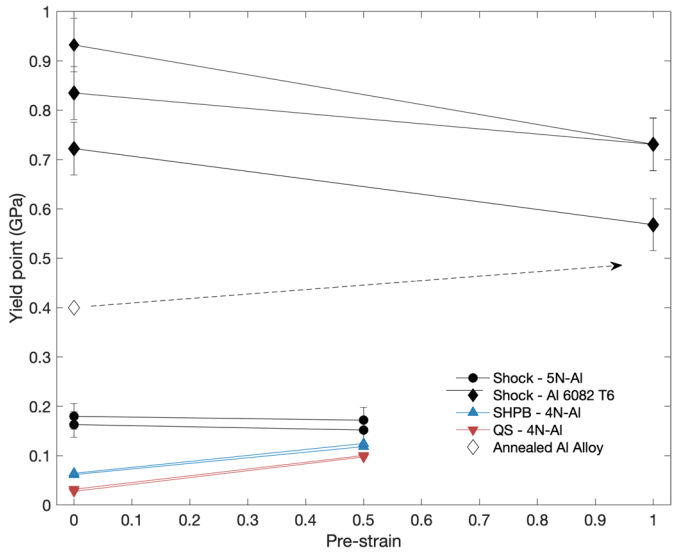

Fig. 11 Relationship between the yield point and pre-applied strain for aluminium in different strain rate regimes. In the low strain rates of quasi-static (QS) and split-Hopkinson pressure bar (SHPB) experiments (literature data from Karnes [73]), increasing the initial dislocation density through cold work produces higher strength. In the high strain rate (shock compression) regime, increasing initial dislocation density leads to higher availability of initial mobile dislocations which can more quickly accommodate plastic deformation (S0 and S1 experiments from the present 5N-Al and Al 6082 data shown, only the 0.6 and 1.0 mm samples have been included for 5N-Al for clarity). If the material is an alloy, annealing will reduce the yield stress as shown (representative data point on annealed Al 5083 taken from Razorenov [19]). Subsequent cold work and/or aging causes an increase in dislocation densities, dislocation pinning and hardening, which strengthens the alloy back towards the yield point of the fully age hardened states (represented by arrow in figure)

density is a primary input parameter [2, 5, 7, 8] will benefit from the additional modelling constraint provided by data such as that presented here, allowing focus to shift further towards investigations of e.g. the role of dislocation generation or annihilation during loading. Experimentally, a natural next step will be to study at which strain rates the material transitions from the low to the high strain rate behaviours depicted in Fig. 11. Clearly, this transition must be material dependent, and in pure aluminium should occur between the strain rates of 10^3 s^{-1} and 10^5 s^{-1}, based on comparisons to SHPB data [73].

Summary

This study presents an investigation into the role of cold work and initial dislocation density in the dynamic strength of aluminium. Plate impact experiments were conducted on pure aluminium and aluminium alloy 6082-T6 with increasing passes of rotary swaging. Detailed material characterisation was performed in order to measure grain size, boundary misorientation, grain orientation, and dislocation density. Comparison of the peak precursor stress states to the measured dislocation densities reveal an inverse relationship, in which increased initial dislocation density results in a faster decay rate and lower peak stresses across all measured thicknesses. While this relationship has long been theorised, detailed quantitative experimental data has been necessary in order to further develop both models and theoretical understanding.

In the high strain rate regime of shock experiments, the high non-equilibrium precursor states are a result of the failure of dislocation mobility alone to relax the imposed deviatoric stresses. The result is a high dependence on dislocation generation, which requires time and high applied stress in order to initiate. Given the experimental results, it is theorised that cold work increases the availability of initial mobile dislocations, which are responsible for increased stress relaxation in the swaged samples and a lessened reliance on generation mechanisms. The findings imply that the increase in mobile dislocations dominates over the effects of increased dislocation pinning when cold worked materials are loaded at high strain rates (above 10^5 s^{-1}), with the opposite being the case in low strain rates (below 10^4 s^{-1}). While the transition to a trend of cold work strengthening should occur before strain rates of around 10^3 s^{-1}, experimental measurement of this shift in Al is still outstanding. Measurement of the transition is of high importance to future work, as it can be used to quantify dislocation mobility, as well as the disparate behaviours of mobile and immobile dislocations as required for dislocation dynamics models.

Acknowledgements The authors would like to thank EPSRC, AWE and DSTL for their support of this research, as well as the technical staff at Imperial College London and the University of Oxford. The authors are also grateful for the sample preparation work by P. Ariyathilaka at Scitech Precision, Harwell. J.C.J. was funded by a joint EPSRC and AWE Industrial CASE Studentship.

Data availability Not applicable.

Declarations

Conflict of interest The authors have no Conflict of interest to declare that are relevant to the content of this article.

References

1. Clifton RJ, Markenscoff X (1981) Elastic precursor decay and radiation from nonuniformly moving dislocations. J Mech Phys Solids 29:227–251. https://doi.org/10.1016/0022-5096(81)90028-4
2. Clayton JD, Lloyd JT (2018) Analysis of nonlinear elastic aspects of precursor attenuation in shock-compressed metallic crystals. J Phys Commun 2:045032. https://doi.org/10.1088/2399-6528/aabc43
3. Gurrutxaga-Lerma B, Balint DS, Dini D, Eakins DE, Sutton AP (2015) Attenuation of the dynamic yield point of shocked aluminum using elastodynamic simulations of dislocation dynamics. Phys Rev Lett 114:1–5. https://doi.org/10.1103/PhysRevLett.114.174301
4. Ding JL, Asay JR, Ao T (2010) Modeling of the elastic precursor behavior and dynamic inelasticity of tantalum under ramp wave loading to 17 GPA. J Appl Phys 107:1–12. https://doi.org/10.1063/1.3373388
5. Austin RA (2018) Elastic precursor wave decay in shock-compressed aluminum over a wide range of temperature. J Appl Phys 10(1063/1):5008280
6. Luscher DJ, Addessio FL, Cawkwell MJ, Ramos KJ (2017) A dislocation density-based continuum model of the anisotropic shock response of single crystal alpha-cyclotrimethylene trinitramine. J Mech Phys Solids 98:63–86. https://doi.org/10.1016/j.jmps.2016.09.005
7. Kositski R, Mordehai D (2019) On the origin of the stress spike decay in the elastic precursor in shocked metals. J Appl Phys 10(1063/1):5110232
8. Kositski R, Mordehai D (2021) A dislocation-based dynamic strength model for tantalum across a large range of strain rates a dislocation-based dynamic strength model for tantalum across a large range of strain rates. J Appl Phys 10(1063/5):0045131
9. Johnson JN, Jones OE, Michaels TE (1970) Dislocation dynamics and single-crystal constitutive relations: shock-wave propagation and precursor decay. J Appl Phys 41:2330–2339. https://doi.org/10.1063/1.1659227
10. Markenscoff X, Clifton RJ (1981) The nonuniformly moving edge dislocation. J Mech Phys Solids 29:253–262. https://doi.org/10.1016/0022-5096(81)90029-6
11. Gurrutxaga-Lerma B, Balint DS, Dini D, Eakins DE, Sutton AP (2013) A dynamic discrete dislocation plasticity method for the simulation of plastic relaxation under shock loading. Proc R Soc A: Math, Phys Eng Sci 469:20130141–20130141. https://doi.org/10.1098/rspa.2013.0141
12. Gurrutxaga-Lerma B, Shehadeh MA, Balint DS, Dini D, Chen L, Eakins DE (2017) The effect of temperature on the elastic precursor decay in shock loaded fcc aluminium and bcc iron. Int J Plast 96:135–155. https://doi.org/10.1016/j.ijplas.2017.05.001
13. Millett JCF, Whiteman G, Park NT, Case S, Bourne NK (2013) The role of cold work on the shock response of tantalum. J Appl Phys 10(1063/1):4810896
14. Razorenov SV, Kanel' GI, Garkushin GV, Ignatova ON (2012) Resistance to dynamic deformation and fracture of tantalum with different grain and defect structures. Phys Solid State 54:790–797. https://doi.org/10.1134/S1063783412040233
15. Asay JR, Ao T, Vogler TJ, Davis JP, Gray GT (2009) Yield strength of tantalum for shockless compression to 18 GPA. J Appl Phys 10(1063/1):3226882
16. Razorenov SV, Savinykh AS, Zaretsky EB, Kanel GI, Kolobov YR (2005) Effect of preliminary strain hardening on the flow stress of titanium and a titanium alloy during shock compression. Phys Solid State 47:663–669. https://doi.org/10.1134/1.1913977
17. Garkushin GV, Ignatova ON, Kanel GI, Meyer LW, Razorenov SV (2010) Submicrosecond strength of ultrafine-grained materials. Mech Solids 45:624–632. https://doi.org/10.3103/S0025654410040114
18. Yu X, Li T, Li L, Liu S, Li Y (2017) Influence of initial texture on the shock property and spall behavior of magnesium alloy az31b. Mater Sci Eng, A 700:259–268. https://doi.org/10.1016/j.msea.2017.06.015
19. Razorenov SV (2018) Influence of structural factors on the strength properties of aluminum alloys under shock wave loading. Matter and Radiat Extrem 3:145–158. https://doi.org/10.1016/j.mre.2018.03.004
20. Brodova IG, Petrova AN, Razorenov SV, Shorokhov EV (2015) Resistance of submicrocrystalline aluminum alloys to high-rate deformation and fracture after dynamic channel angular pressing. Phys Met Metall 116:519–526. https://doi.org/10.1134/S0031918X15050051
21. Ivanov KV, Razorenov SV, Garkushin GV (2018) Quasi-static and shock-wave loading of ultrafine-grained aluminum: effect of microstructural characteristics. J Mater Sci 53:14681–14693. https://doi.org/10.1007/s10853-018-2619-3
22. Whelchel RL, Thadhani NN, Sanders TH, Kecskes LJ, Williams CL (2014) Spall properties of al 5083 plate fabricated using equi-channel angular pressing (ECAP) and rolling. J Phys: Confer Ser. https://doi.org/10.1088/1742-6596/500/11/112066
23. Kamikawa N, Huang X, Tsuji N, Hansen N (2009) Strengthening mechanisms in nanostructured high-purity aluminium deformed to high strain and annealed. Acta Mater 57:4198–4208. https://doi.org/10.1016/j.actamat.2009.05.017
24. Chinh NQ, Szommer P, Horita Z, Langdon TG (2006) Experimental evidence for grain-boundary sliding in ultrafine-grained aluminum processed by severe plastic deformation. Adv Mater 18:34–39. https://doi.org/10.1002/adma.200501232

25. Ito Y, Horita Z (2009) Microstructural evolution in pure aluminum processed by high-pressure torsion. Mater Sci Eng, A 503:32–36. https://doi.org/10.1016/j.msea.2008.03.055
26. Yadav D, Bauri R (2012) Effect of friction stir processing on microstructure and mechanical properties of aluminium. Mater Sci Eng, A 539:85–92. https://doi.org/10.1016/j.msea.2012.01.055
27. Ham RK (1961) The determination of dislocation densities in thin films. Phil Mag 6:1193–1194. https://doi.org/10.1080/14786436108239679
28. Gubicza J, Chinh NQ, Krállics G, Schiller I, Ungár T (2006) Microstructure of ultrafine-grained fcc metals produced by severe plastic deformation. Curr Appl Phys 6:194–199. https://doi.org/10.1016/j.cap.2005.07.039
29. Kamikawa N, Tsuji N, Huang X, Hansen N (2006) Quantification of annealed microstructures in arb processed aluminum. Acta Mater 54:3055–3066. https://doi.org/10.1016/j.actamat.2006.02.046
30. Miyajima Y, Mitsuhara M, Hata S, Nakashima H, Tsuji N (2010) Quantification of internal dislocation density using scanning transmission electron microscopy in ultrafine grained pure aluminium fabricated by severe plastic deformation. Mater Sci Eng, A 528:776–779. https://doi.org/10.1016/j.msea.2010.09.058
31. Zhilyaev AP, Gimazov AA, Langdon TG (2013) Recent developments in modelling of microhardness saturation during spd processing of metals and alloys. J Mater Sci 48:4461–4466. https://doi.org/10.1007/s10853-013-7155-6
32. Williams CL, Chen CQ, Ramesh KT, Dandekar DP (2014) On the shock stress, substructure evolution, and spall response of commercially pure 1100-o aluminum. Mater Sci Eng, A 618:596–604. https://doi.org/10.1016/j.msea.2014.09.030
33. Meyers MA, Jarmakani H, Bringa EM, Remington BA (2009) Dislocations in solids, vol 15. Elsevier, pp 91–197. https://doi.org/10.1016/S1572-4859(09)01502-2
34. Yang Y, Nie J, Mao Q, Zhao Y (2019) Improving the combination of electrical conductivity and tensile strength of al 1070 by rotary swaging deformation. Results Phys 13:102236. https://doi.org/10.1016/j.rinp.2019.102236
35. El-Madhoun Y, Mohamed A, Bassim MN (2003) Cyclic stress-strain response and dislocation structures in polycrystalline aluminum. Mater Sci Eng, A 359:220–227. https://doi.org/10.1016/S0921-5093(03)00347-2
36. Kumar N, Rao PN, Jayaganthan R, Brokmeier HG (2015) Effect of cryorolling and annealing on recovery, recrystallisation, grain growth and their influence on mechanical and corrosion behaviour of 6082 al alloy. Mater Chem Phys 165:177–187. https://doi.org/10.1016/j.matchemphys.2015.09.014
37. Hu R, Ogura T, Tezuka H, Sato T, Liu Q (2010) Dispersoid formation and recrystallization behavior in an Al–Mg–Si–Mn alloy. J Mater Sci Technol 26:237–243. https://doi.org/10.1016/S1005-0302(10)60040-0
38. Kumar N, Goel S, Jayaganthan R, Owolabi GM (2018) The influence of metallurgical factors on low cycle fatigue behavior of ultra-fine grained 6082 al alloy. Int J Fatigue 110:130–143. https://doi.org/10.1016/j.ijfatigue.2018.01.018
39. Cabibbo M, Evangelista E, Vedani M (2005) Influence of severe plastic deformations on secondary phase precipitation in a 6082 Al–Mg–Si alloy. Metall Mater Trans A 36:1353–1364. https://doi.org/10.1007/s11661-005-0226-9
40. Liu M, Roven HJ, Yu Y, Werenskiold JC (2008) Deformation structures in 6082 aluminium alloy after severe plastic deformation by equal-channel angular pressing. Mater Sci Eng, A 483–484:59–63. https://doi.org/10.1016/j.msea.2006.09.144
41. Liu XC, Zhang HW, Lu K (2013) Strain-induced ultrahard and ultrastable nanolaminated structure in nickel. Science 342:337–340. https://doi.org/10.1016/j.jallcom.2017.08.018
42. Miyajima Y, Ueda T, Adachi H, Fujii T, Onaka S, Kato M (2014) Dislocation density of fcc metals processed by arb. IOP Confer Ser: Mater Sci Eng. https://doi.org/10.1088/1757-899X/63/1/012138
43. Torre FD, Lapovok R, Sandlin J, Thomson PF, Davies CH, Pereloma EV (2004) Microstructures and properties of copper processed by equal channel angular extrusion for 1–16 passes. Acta Mater 52:4819–4832. https://doi.org/10.1016/j.actamat.2004.06.040
44. Dolan DH, Ao T, Hernandez O (2012) Note: Frequency-conversion photonic doppler velocimetry with an inverted circulator. Rev Sci Instrum. https://doi.org/10.1063/1.3688851
45. Strand OT, Goosman DR, Martinez C, Whitworth TL, Kuhlow WW (2006) Compact system for high-speed velocimetry using heterodyne techniques. Rev Sci Instrum. https://doi.org/10.1063/1.2336749
46. Millett JC, Whiteman G, Bourne NK (2009) Lateral stress and shear strength behind the shock front in three face centered cubic metals. J Appl Phys. https://doi.org/10.1063/1.3077206
47. Zaretsky EB, Kanel GI (2012) Effect of temperature, strain, and strain rate on the flow stress of aluminum under shock-wave compression. J Appl Phys. https://doi.org/10.1063/1.4755792
48. Whitley VH, McGrane SD, Eakins DE, Bolme CA, Moore DS, Bingert JF (2011) The elastic-plastic response of aluminum films to ultrafast laser-generated shocks. J Appl Phys 109:4–7. https://doi.org/10.1063/1.3506696
49. Gupta YM, Winey JM, Trivedi PB, Lalone BM, Smith RF, Eggert JH, Collins GW (2009) Large elastic wave amplitude and attenuation in shocked pure aluminum. J Appl Phys 105:2009–2011. https://doi.org/10.1063/1.3075839
50. Winey JM, Lalone BM, Trivedi PB, Gupta YM (2009) Elastic wave amplitudes in shock-compressed thin polycrystalline aluminum samples. J Appl Phys 106:3–7. https://doi.org/10.1063/1.3236654
51. Arvidsson TE, Gupta YM, Duvall GE (1975) Precursor decay in 1060 aluminum. J Appl Phys 46:4474–4478. https://doi.org/10.1063/1.321423
52. Smith RF, Eggert JH, Rudd RE, Swift DC, Bolme CA, Collins GW (2011) High strain-rate plastic flow in al and fe. J Appl Phys. https://doi.org/10.1063/1.3670001
53. Davis JP (2006) Experimental measurement of the principal isentrope for aluminum 6061-t6 to 240 GPa. J Appl Phys. https://doi.org/10.1063/1.2196110
54. Johnson JN, Barker LM (1969) Dislocation dynamics and steady plastic wave profiles in 6061-t6 aluminum. J Appl Phys 40:4321–4334. https://doi.org/10.1063/1.1657194
55. Lipkin J, Asay JR (1977) Reshock and release of shock-compressed 6061-t6 aluminum. J Appl Phys 48:182–189. https://doi.org/10.1063/1.323306
56. Sakino K (2000) Transition in rate controlling mechanism of fcc metals at very high strain rates and high temperatures. J Phys 10. https://doi.org/10.1051/jp4:2000910
57. Zaretsky EB, Frage N, Kalabukhov S (2019) Shock wave determination of the strengthening of commercial aluminum alloy 6061 by point defects. Mater Sci Eng, A 761:138066. https://doi.org/10.1016/j.msea.2019.138066
58. Zaretsky EB, Kanel GI (2014) Tantalum and vanadium response to shock-wave loading at normal and elevated temperatures. Non-monotonous decay of the elastic wave in vanadium. J Appl Phys. https://doi.org/10.1063/1.4885047
59. Meyer LW, Hockauf M, Kröger L, Schneider I (2007) Compressive behaviour of ultrafine-grained aa6063t6 over a wide

range of strains and strain rates. Z Metall/Mater Res Adv Techn 98:191–199
60. Brodova I, Petrova A, Kreitcberg A, Prokoshkin S (2017) The influence of the structure of ultrafine-grained aluminium alloys on their mechanical properties under dynamic compression and shock-wave loading the influence of the structure of ultrafine-grained aluminium alloys on their mechanical properties under. J Phys: Confer Ser 894:012016. https://doi.org/10.1088/1742-6596/894/1/012016
61. Whelchel RL, Kennedy GB, Dwivedi SK, Sanders TH, Thadhani NN (2013) Spall behavior of rolled aluminum 5083-h116 plate. J Appl Phys 10(1063/1):4811452
62. Mouritz AP (2012) Introduction to aerospace materials. American Institute of Aeronautics and Astronautics, Reston. https://doi.org/10.2514/4.869198
63. Millett JCF, Bourne NK, Chu MQ, Jones IP, Gray GT, Appleby-Thomas G (2010) The role of aging on the mechanical and microstructural response of aluminum 6061 to one-dimensional shock loading. J Appl Phys 108:1–9. https://doi.org/10.1063/1.3490135
64. Millett JCF, Bourne NK, Park NT, Whiteman G, Gray GT (2011) On the behaviour of body-centred cubic metals to one-dimensional shock loading. J Mater Sci 46:3899–3906. https://doi.org/10.1007/s10853-011-5311-4
65. Owen GD, Chapman DJ, Whiteman G, Stirk SM, Millett JCF, Johnson S (2017) Spall behaviour of single crystal aluminium at three principal orientations. J Appl Phys 122:155102. https://doi.org/10.1063/1.4999559
66. Huang H, Asay JR (2006) Reshock response of shock deformed aluminum. J Appl Phys 10(1063/1):2266234
67. Pope L, Johnson J (1975) Shockwave compression of single crystal beryllium. J Appl Phys 46:720–729. https://doi.org/10.1063/1.321636
68. Jonsson JC, Chapman DJ, Farbaniec L, Escauriza EM, Smith LC, Eakins DE (2023) Role of crystal orientation in the dynamic strength of magnesium alloy az31b. JOM. https://doi.org/10.1007/s11837-023-05967-4
69. Jonsson JC (2021) Studies on the role of microstructure in the dynamic strength of metals. PhD thesis, University of Oxford
70. Asay JR, Ao T, Davis JP, Hall C, Vogler TJ, Gray GT (2008) Effect of initial properties on the flow strength of aluminum during quasi-isentropic compression. J Appl Phys. https://doi.org/10.1063/1.2902855
71. Trivedi PB, Asay JR, Gupta YM, Field DP (2007) Influence of grain size on the tensile response of aluminum under plate-impact loading. J Appl Phys. https://doi.org/10.1063/1.2798497
72. Huang H, Asay JR (2005) Compressive strength measurements in aluminum for shock compression over the stress range of 4-22 GPa. J Appl Phys. https://doi.org/10.1063/1.2001729
73. Karnes CH, Ripperger EA (1966) Strain rate effects in cold worked high-purity aluminium. J Mech Phys Solids 14:75–88. https://doi.org/10.1016/0022-5096(66)90038-X